Supporting Information

Adaptive ionic skin with multiple stimulus responses and moist-electric generation talent

Xiaofeng Pan[a1], Qinhua Wang[a1], Runsheng Guo[a], Shilin Cao[a], Hui Wu[a], Xinhua Ouyang[a], Fang Huang[a], Haili Gao[a], Liulian Huang[a], Fan Zhang[b], Lihui Chen[a]*, Yonghao Ni[a,c]*, Kai Liu[a]*

[a] College of Material Engineering, Fujian Agriculture and Forestry University, Fuzhou City, Fujian Province 350002, People's Republic of China

[b] School of Chemistry and Chemical Engineering, Shanghai Jiao Tong University, State Key Laboratory of Metal Matrix Composites, 800 Dongchuan Road, Shanghai, 200240, People's Republic of China

[c] Limerick Pulp and Paper Centre, Department of Chemical Engineering, University of New Brunswick, Fredericton, New Brunswick E3B5A3, Canada

Experimental section

Materials

Polyvinyl alcohol (PVA) (degree of polymerization: 1700; degree of alcoholysis: 99%), anhydrous calcium chloride ($CaCl_2$) and glycerol were provided by Aladdin Industrial Corporation (Shanghai, China). The cellulose nanofibrils (CNFs, 0.83 wt %) oxidized by TEMPO-mediated oxidation were provided by Haojia Cellulose Co., Ltd. (Tianjin, China). Unless otherwise stated, the above materials were not further purified for use.

Preparation of the ion-conducting organohydrogel (ICOH)

First, 10 ml of glycerol and 10 ml of deionized water were uniformly mixed to prepare a binary solvent. Then, 1 g of CNFs and 0.22 g of $CaCl_2$ were uniformly dispersed in the above solvent system while mixing/stirring via ultrasonic means. Then, 3.39 g of PVA powder was added to the above mixed solution and dissolved by heating the solution to 95°C. Finally, the reaction solution was quickly poured into a polytetrafluoroethylene (PTFE) mold article, frozen overnight, and then subjected to freezing-thawing at room temperature for 6 h to obtain ion-conducting organohydrogels (ICOH). Finally, the gel was placed in a 4 °C refrigerator for later use. At the same time, PVA-CNFs-$CaCl_2$ hydrogel without glycerol was also prepared for comparison.
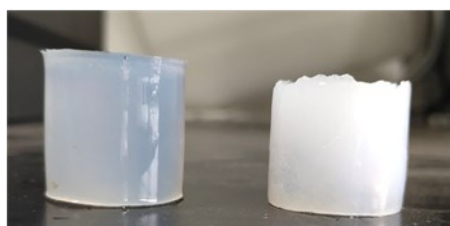
Schematic S1. Photograph of PVA organohydrogel and PVA hydrogel.

Characterization of the ion-conducting organohydrogel (ICOH)

The ICOH was placed in deionized water and repeatedly soaked to displace the internal glycerol. Next, the glycerol-removed hydrogel was freeze-dried and observed by a scanning electron microscope (Thermo scientific Verios G4 UC, USA). The UV-vis spectra (200-850 nm) and haze (350-800 nm) of the ICOH (thickness: 1.5 mm) were carried out using Lambda 750 S. The freezing temperature of the ICOH was determined using differential scanning calorimetry (DSC 214, Netsch) in the temperature range of 20 to -120°C. The flaky and cylindrical ICOH and PVA hydrogels with or without the VHB package were placed in a constant temperature and humidity room (25°C, 50% RH) for anti-dryness studies. A digital tensile machine (KJ-1065B, Kejian Instrument Co. Ltd, Dongguan, China) at a loading rate of 50 mm/min, was used to characterize the uniaxial tensile behaviors of the ICOH. The Young's modulus (E) of the ICOH was calculated from the slope of the 5-20% strain region in the stress-strain curve. The toughness (T) of the ICOH was estimated by the area under the stress-strain curve from 0% strain to the fracture strain (ζ_β) using the following equation:

$$T = \int_0^{\zeta_\beta} \sigma(\zeta)d\zeta \qquad (1)$$

The softness of the ICOH (T: 1.5 mm) and other test materials was measured using a leather softness tester (Dongguan Gaoxin Testing Equipment Co., Ltd. China).

The conductivity of gel was measured by an LCR meter (TH 2832), the applied voltage was 1 V and the measuring frequency was 1 kHz. The conductivity (σ) was calculated using the following equation:

$$\sigma = L/RA \qquad (2)$$

Where R is the resistance, L and A are the materials' length and cross-sectional area, respectively.

The thickness of the above materials was measured by a thickness tester (GuangLu Guilin, China). The flaky ICOH was placed in an oven (110°C) to completely evaporate the binary solvent, and the element distribution of the ICOH was mapped on an Octane Elect EDS | (EDAX, USA). The thermal self-healing properties of the ICOH substrate material were also studied. Thermal imaging technology was provided by FLIRONE® PRO (USA).

Preparation and characterization of the strain-sensitive component (SSC) and adaptive kirigami-inspired sensor

The precursor solution of the ICOH was placed in different molds and pre-customized in different ICOH shapes, such as elephants, octagons, bears, and a heart. Similarly, the ICOH can be dyed using hydrophilic dyes of different colors according to individual preferences. The customized ICOH was connected to copper foil and an LCR meter to assemble a resistive strain-sensitive component (SSC). The customized SSC was attached to a hand model (silicone) to explore the SSC's ability to respond to pressure. The ICOH was cut to prepare a kirigami ICOH and assemble the kirigami sensor. The mechanical, wearable, and sensing properties of the kirigami ICOH and kirigami sensor were also studied. Commercial Finite Element software (ABAQUS) was used to simulate the local unit strain of the kirigami ICOH.

The strain sensitivity of the sensor was evaluated by the gauge factor (GF), which was

defined as the ratio of relative resistance change to applied strain (α).

$$GF = [(R - R_0)/R_0]/\alpha \quad (3)$$

Where R_0 and R are resistances at 0% strain and under stretching, respectively.

Preparation and characterization of the temperature-sensitive component (TSC)

The strip ICOH ($3\times1\times0.15$ cm^3) was connected to conductive wires and an LCR meter (TH2832, Changzhou China) to assemble the temperature-sensitive component (TSC). The data was recorded with a customized LabView program. The heat was produced using a hair dryer (Philips, Netherlands), and the PT1000 temperature sensor was used to detect the temperature. The cooling process was performed in a refrigerator (BOSHI, Germany), and the temperature was calibrated using a hand-held IR THERMOMETER (MT4 MAX+, FLUKE USA).

Preparation and characterization of the humidity-sensitive component (HSC)

The strip ICOH ($3\times1\times0.15$ cm^3) was connected to conductive wire and an LCR meter (TH2832, Changzhou China) to assemble the humidity-sensitive component (HSC). The humidity was controlled using a homemade humidity-generating device and flow meter to simulate a dynamic humidity environment (unless otherwise noted, the temperature of the moisture was close to room temperature).

Preparation and characterization of the moist-electric-generating component (MEGC)

The bottom of the ICOH (4×6 cm^2) was attached to the VHB, and the top was exposed to air to prepare the moist-electric-generating component (MEGC). The upper and lower surfaces of the ICOH were connected in series on a multimeter (UT890D+, UNI-

T CHINA) or electrochemical workstation (CHI 630E) through copper foil for real-time detection of DC potential. A humidifier (Rongshen, China), human exhalation and air moisture were used as moisture sources to study the MEGC's moist-electric-generating mechanism and performance. Moreover, the UV−vis absorption and ATR-FTIR spectra of the ICOH before and after humidification were recorded.

Preparation and application of the moist-electric-generating ionic skin

The above components were assembled into a moist-electric-generating ionic skin that can detect temperature, pressure, strain, and humidity.

Theoretical Section

1. Computational methods

To understand the details of the interaction between CNFs and PVA, we performed the first-principle calculations using the DMol[3] program in Materials Studio.[1,2] The exchange-correlation functional was treated by the generalized gradient approximation (GGA) with the PW91 parameterization.[3] We used OBS method for DFT-D correction to refine noncovalent interactions such as hydrogen bonding.[4] All systems were fully relaxed with symmetry. All-electron treatment and double numerical basis including d- and p-polarization function (DNP) [1] were used. The relaxation of atomic positions was considered to be converged when the change in total energy is less than 1.0×10^{-5} Ha/Å, and the force on each atom is less than 0.002 Ha/Å.

2. Structural models

Since PVA molecules could only touch a few cellulose chains on the surface of CNFs, we have employed the cellobiose and PVA monomer to construct models of the composite system in our study. Figure S1a displays the atomic structures of water, glycerol, PVA monomer and cellobiose. It is easy to form intramolecular hydrogen bonds for glycerol and cellobiose, and intermolecular hydrogen bonds for water. Starting from the basic atomic structures, we have respectively investigated the composite configurations of the cellobiose and PVA monomer adsorbed with water and glycerol molecules, as shown in Figure S1b, S2. The structures of cellobiose and PVA in the mixed solvent of water and glycerol are also studied based on DFT calculations, which display different bonding strength from water solvent.
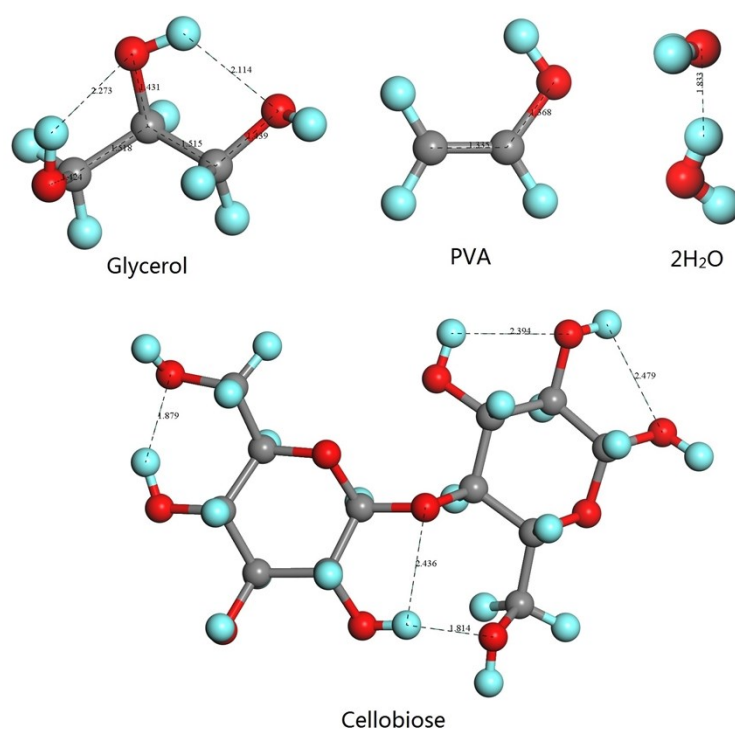
Figure S1a. Energy favorable configurations of glycerol, PVA monomer, 2H$_2$O and cellobiose. The grey balls represent C atoms, red balls highlight O atoms, and light blue

balls represent H atoms. Black dotted lines and numbers represent hydrogen bonds and bond length in unit of Å, respectively.

3. Stability of cellobiose and PVA composite system.

The stability of cellobiose and PVA composite system can be described by the binding energy E_b of the molecules defined as:

$$E_b(n) = E_{com} - E_m - E_{others} \tag{4}$$

where E_{com} is the total energies of the composite system, and E_m is the total energies of the investigated molecule. E_{others} is the total energy of other components excluding the investigated molecule in composite system. For example, E_m and E_{others} represent total energy of PVA monomer and Cellobiose/16H$_2$O in calculating binding energy of PVA monomer adsorbed on the cellobiose in water solvent, respectively. The negative value of binding energy indicates the formation of composite system exothermic. The computed binding energy between water molecules is -0.413 eV, between the previous theoretical values of 0.275 eV and -1.551 eV at GGA-PBE/DNP(3.5) level using the Dmol^3 program.[5,6]

4. Equilibrium configurations and binding energy of water-water, glycerol-water and glycerol-glycerol system.

As shown in figure S1b, the glycerol-glycerol and glycerol-water interactions are stronger than that of water-water systems, which can be ascribed to more hydroxyl groups in glycerol, benefitting the formation of hydrogen bonds between glycerol and other molecules. The binding energy between glycerol molecules depends sensitively

on the spatial configurations of touching glycerol molecules, which was often neglected in previous studies.[5,6] For example, there is one more hydrogen bond formed in 2Glycerol-type II configuration with binding energy of -1.334 eV than that in 2Glycerol-type I configuration with -0.696 eV, resulting in binding energy difference of -0.638 eV. The higher stability of water/glycerol coexisting systems observed in experiments could be related to the competitive glycerol-water binding energy and higher mobility of water molecules than glycerol molecules.

(a)

(b)

2H$_2$O: -0.414 eV

Glycerol/H$_2$O: -0.977 eV

(c)

(d)

2Glycerol-type I: -0.696 eV

2Glycerol-type II: -1.334 eV
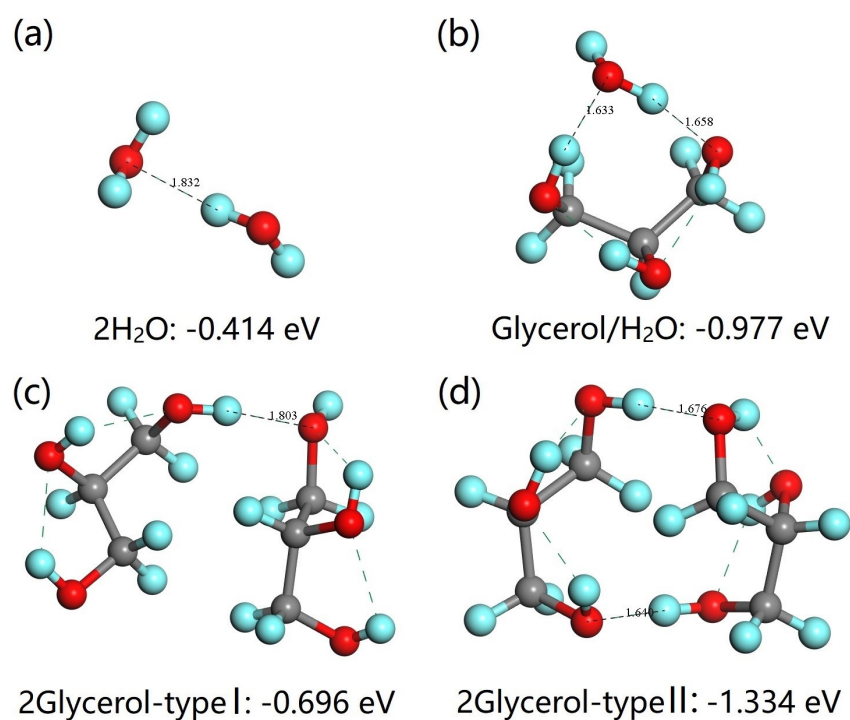
Figure S1b. Energy favorable configurations of (a) 2H$_2$O, (b) H$_2$O and glycerol, (c) type I and (d) type II of two glycerol molecules. The grey balls represent C atoms, red balls highlight O atoms, and light blue balls represent H atoms. Black dotted lines and numbers represent hydrogen bonds and bond length in unit of Å, respectively. Green dotted lines represent intramolecular H bonds or H bonds between water molecules.

5. Equilibrium configurations and binding energy of cellobiose adsorbed with H$_2$O, glycerol and PVA monomer.

Figure S2a shows the energy favorable configurations of H$_2$O, glycerol and PVA adsorbed in pristine and hydrated cellobiose. Due to cellulose containing abundant hydroxyl groups, both glycerol and PVA could bond strongly with it through forming intermolecular hydrogen bonds, especially in water solvent. The binding energy between glycerol and cellobiose is -2.038 eV, stronger than that of H$_2$O and PVA, which implies the interactions between cellobiose and other molecules depending on the number of intermolecular hydrogen bonds. The existence of water molecules around the cellobiose can enhance the interactions between the cellobiose and PVA monomer with the binding energy increasing by about -0.451 eV. The same phenomenon also happens to glycerol, and the binding energy between glycerol and cellobiose is raised by about -2.170 eV in water solvent compared to anhydrous environment.
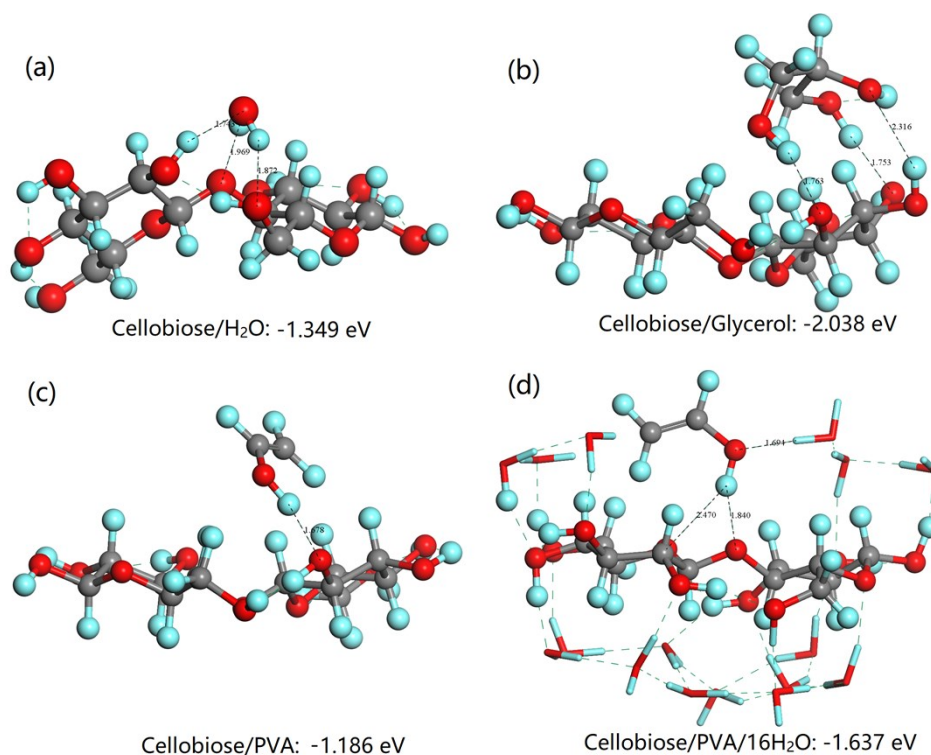
Figure S2a. Energy favorable configurations of the cellobiose adsorbed with (a) H_2O, (b) glycerol, (c) PVA monomer and (d) hydrated PVA monomer. The grey balls represent C atoms, red balls (or sticks) highlight O atoms, and light blue balls (or sticks) represent H atoms. Black dotted lines and numbers represent hydrogen bonds and bond length in unit of Å, respectively. Green dotted lines represent intramolecular H bonds or H bonds between water molecules.

6. **Equilibrium configurations and binding energy of PVA monomer adsorbed with glycerol, H_2O and cellobiose.**

The interaction between PVA and cellobiose molecules is stronger than that between PVA and glycerol (or water) molecules, as shown in figure S2b. Glycerol and PVA molecules can both improve the stability of PVA and cellobiose composite configuration with the binding energy increasing by more than 1.1 eV. The presence of

glycerol molecules raises the binding energy between PVA and cellobiose even more compared with water as the only solvent, indicating that composite system of CNFs and PVA can profit from the glycerol/water binary solvent system than the use of water as the only solvent.
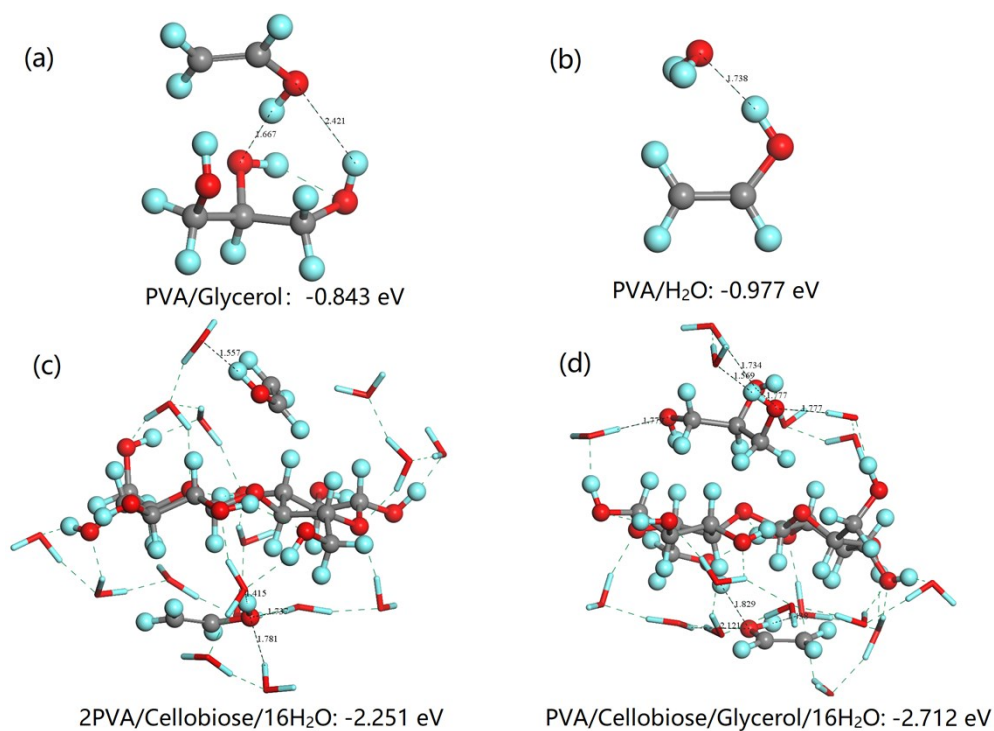

Figure S2b. Energy favorable configurations of the PVA monomer adsorbed with (a) glycerol, (b) H_2O, (c) PVA/cellobiose/16H_2O and (d) cellobiose/glycerol. The grey balls represent C atoms, red balls (or sticks) highlight O atoms, and light blue balls (or sticks) represent H atoms. Black dotted lines and numbers represent hydrogen bonds and bond length in unit of Å, respectively. Green dotted lines represent intramolecular H bonds or H bonds between water molecules.
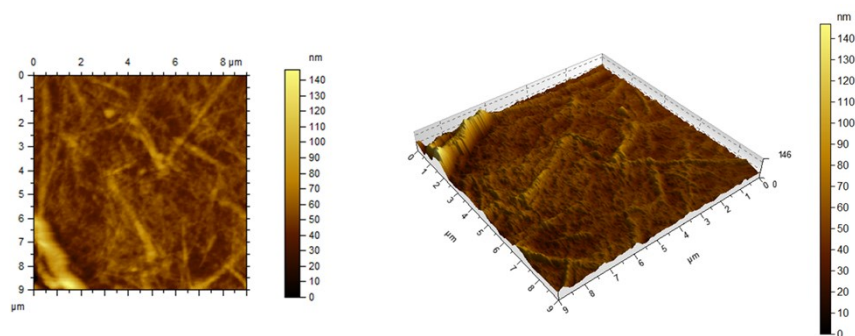
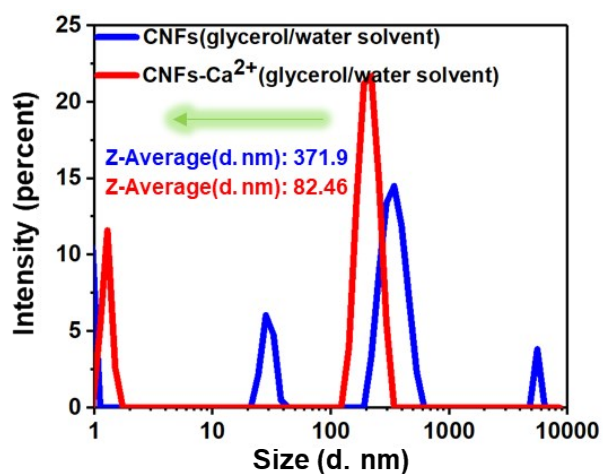**Figure S3.** The CNFs morphology obtained using AFM (Multimode 8, Bruker).

Figure S4. The size of CNFs and CNFs-Ca^{2+} assemblies in glycerol/water binary solvent determined using a Malvern Zetasizer (Nano ZS90, UK).

The haze can be calculated according to the following formula:

$$Haze(\%) = \left(\frac{T_4}{T_2} - \frac{T_3}{T_1}\right) \times 100\%$$

(5)

T_1 refers to incident light; T_2 refers to the total light transmittance of the sample; T_3 refers to light scattering caused by the device; and T_4 refers to light scattering caused by the sample and equipment.

Figure S5. The photograph of the Ca^{2+}-CNFs assembly suspension.

Fracture elongation (%)	445 ±20
Fracture strength (MPa)	0.59 ±0.019
Young's modulus (kPa)	276 ±8.78
Toughness (MJ/m^3)	1.478 ±0.086

Figure S6. The mechanical properties of the ICOH.

The softness measurement was performed to evaluate the adaptability of devices. For a better comparison, some common substrate materials and ICOH were selected. The higher the softness (mm), the better the flexibility and wearability of the material. Surprisingly, despite the high thickness of the ICOH sample (1.5 mm), its softness is still as high as 8.2 mm, which is as soft as a napkin. The good balance of mechanical properties and softness of ICOH can be attributed to the unique advantages of ionic gels. Generally, the strength of the gel is lower than that of the polymer composites and metals, even cellulose paper. Overall, the ICOH has high softness, thus, exhibiting excellent adaptability.
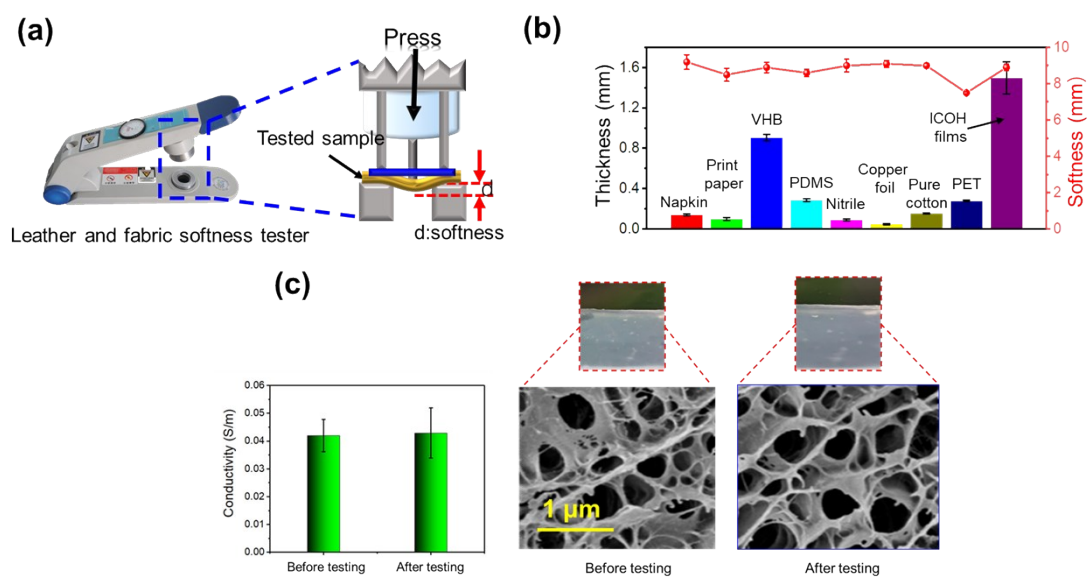
Figure S7. a) Photograph of the softness tester (leather and fabric softness tester) and schematic illustration for measuring softness. b) Thickness and softness of various flexible substrate materials. c) Conductivity and structure of ICOH before and after softness testing.
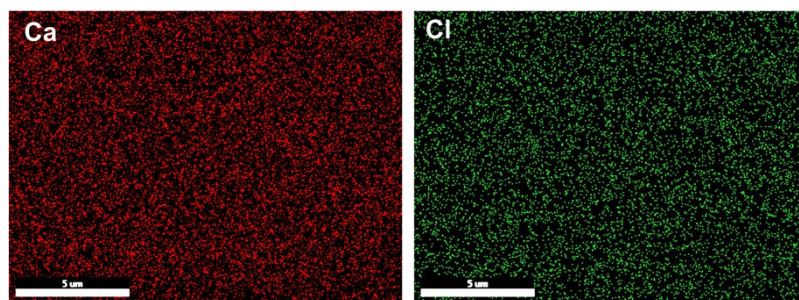

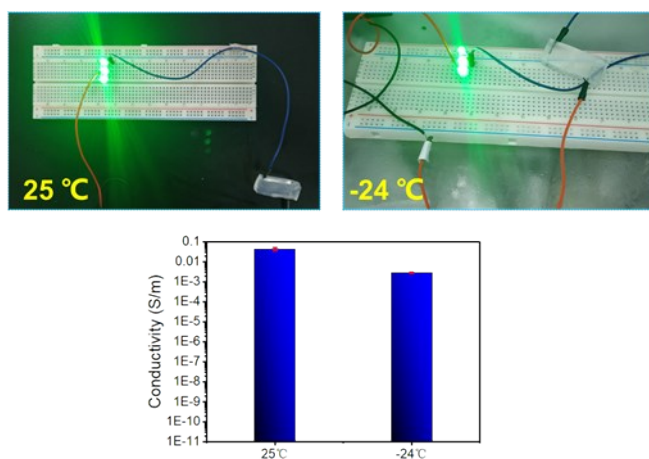**Figure S8.** Calcium and chlorine elemental mapping of solvent-free ICOH.

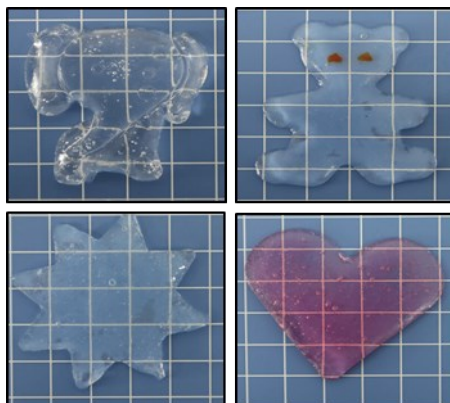**Figure S9.** The ionic conductive ICOH can illuminate three LED bulbs at 25℃ and

-24℃.

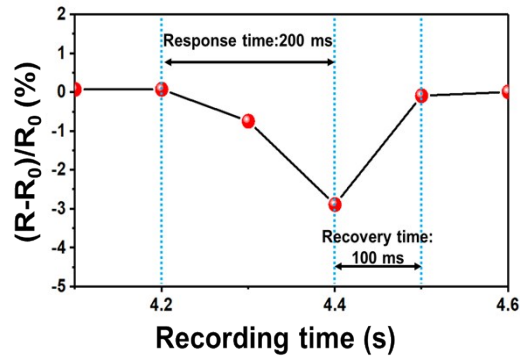**Figure S10.** Different shapes and colors of ICOH.

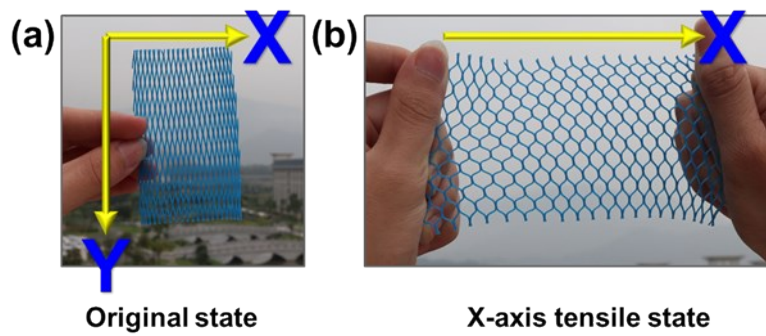**Figure S11.** The SSC pressure response and recovery time.

Figure S12. A rigid body with a kirigami structure can be easily stretched on the X-axis.
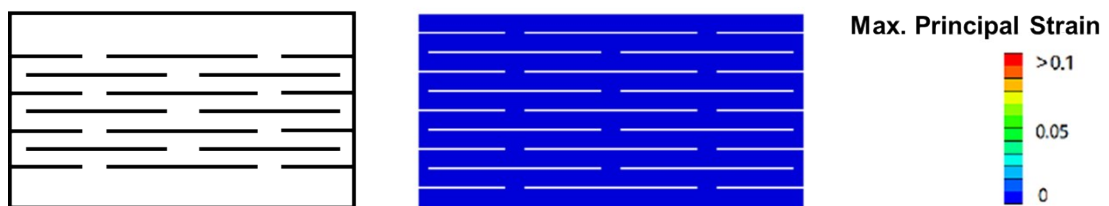

Figure S13. The kirigami ICOH design with alternating parallel lines (0% strain).
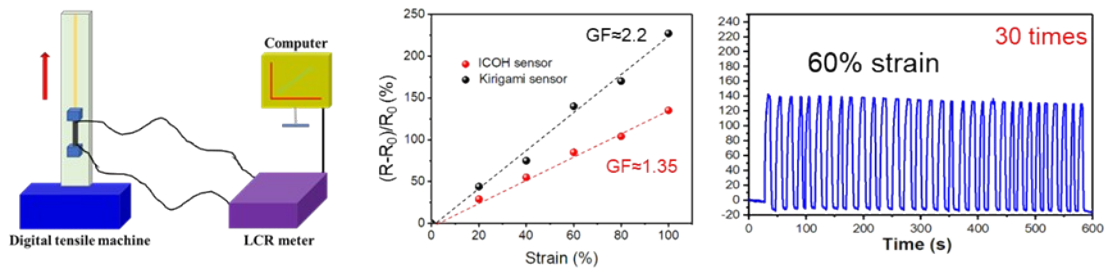
Figure S14. The gauge factor (GF) of ICOH sensor and kirigami sensor, and strain-sensing stability of kirigami sensor.
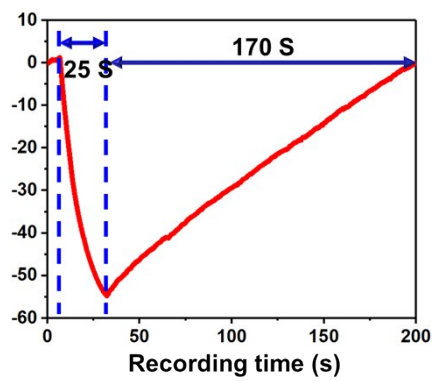

Figure S15. Temperature response and recovery time of TSC in response to temperature increasing.

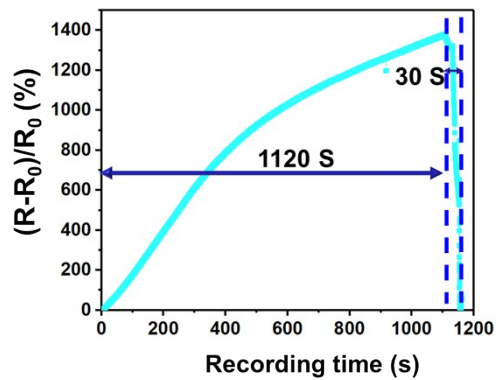**Figure S16.** Temperature response and recovery time of TSC in response to temperature decreasing.
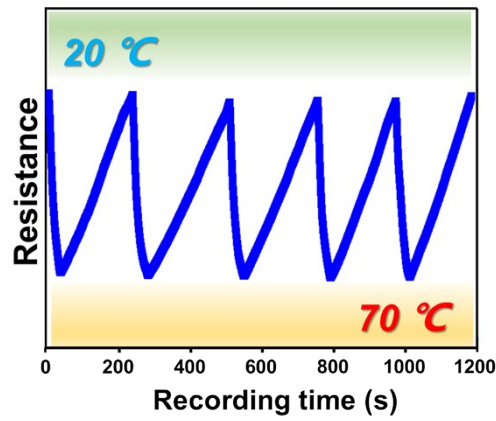
Figure S17. Dynamic responses of the TSC from 20°C to 70°C in 5 experimental cycles.
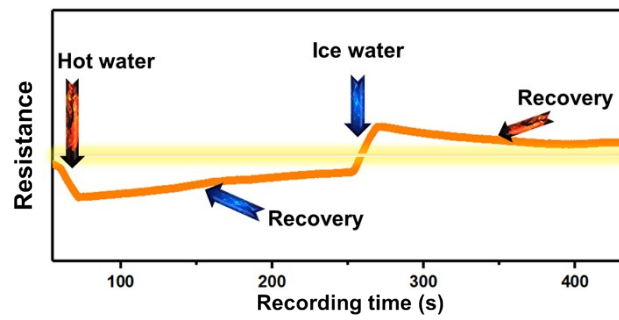
Figure S18. Temperature response process of TSC to hot and cold water during one test.

Figure S19. Relative resistance variation of moisture isolated HSC under low temperature moisture (10°C) cooling.
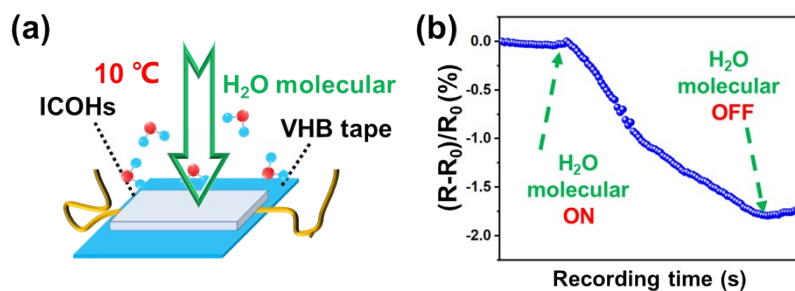
Figure S20. The relative resistance variation of the HSC in direct moisture (10°C) contact cooling.
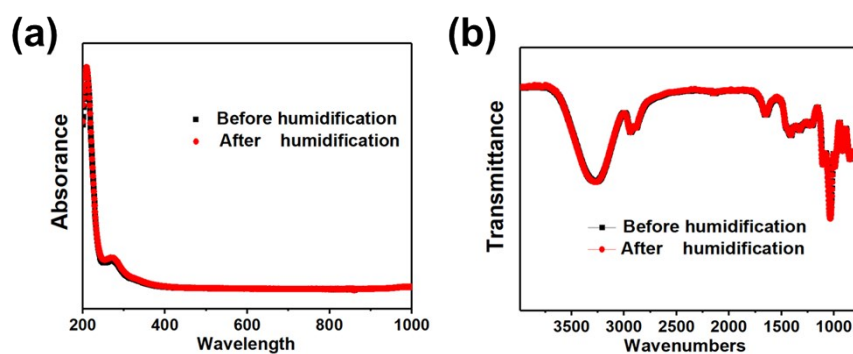
Figure S21. The a) UV−vis absorption and b) FTIR spectra of the ICOH before and after humidification.
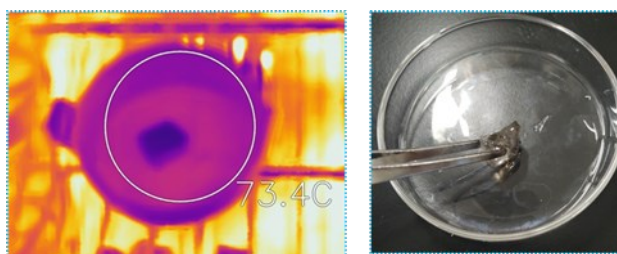
Figure S22. Photograph of the thermoplastic behavior of the ICOH.
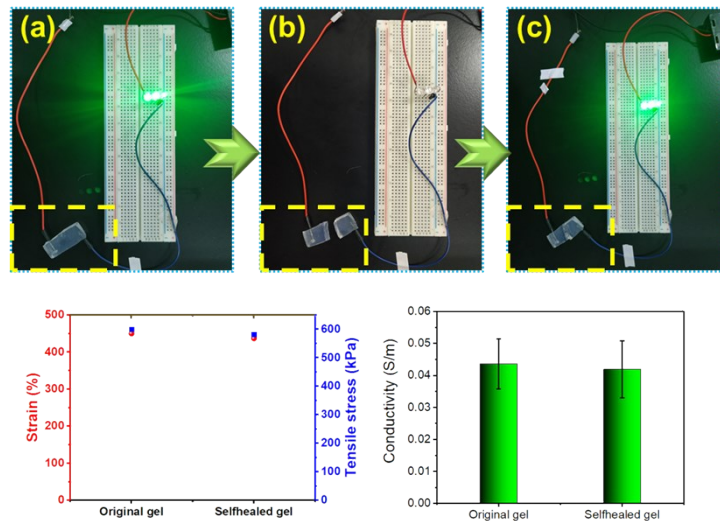
Figure S23. The thermal self-healing behavior and capability of ICOH.

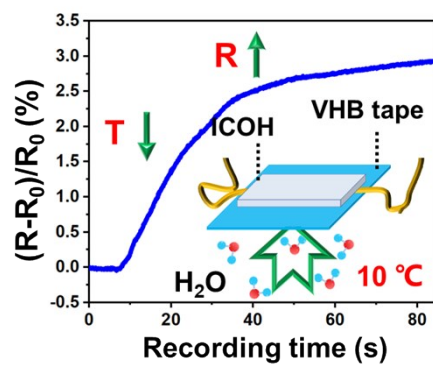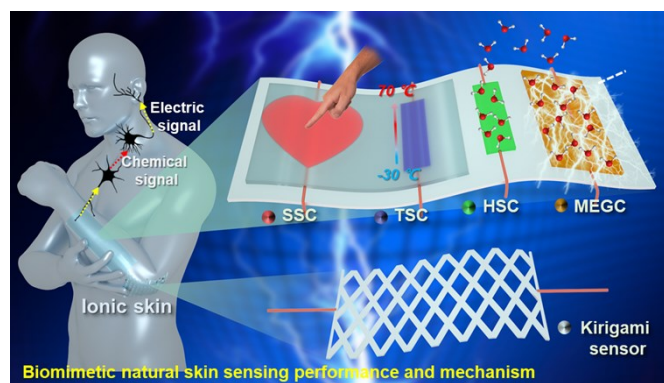| Polymer (Conductive materials)	Stretchable	Transparent	Strain/pressure-sensitive	Temperature-sensitive	Humidity-sensitive	Self-powered	Re-shapeable
PVA(PANI)[6]	★		★				★
PVA(PEDOT:PSS)[7]	★		★				★
PVA(Al^{3+})[8]	★	★	★				
PAAm(MAANa)[9]	★	★	★				
P(AM-co-AA)(CNTs)[5]	★		★				
PAA(PEDOT:SL)[10]	★		★				
Guar gum(Na^{+})[11]	★		★				
k-carrageenan/PAM（K^{+}）[12]	★	★	★	★	★		
PVA(Ca^{2+})	★	★	★	★	★	★	★

Figure S24. Performance comparison between the ICOH and recent organohydrogel sensors based on the binary solvent system (the five-pointed star refers to sensor with this performance, and the blank represents none or not mentioned).

Table S1. Comparison of reported skin-like hydrogels with our work in structure and sensing mimicking of nature skin (selected from publications in top journals (IF> 10)).

Components for recently skin-like gels	Anti-dryness	Anti-freeze	Haze	Stretchability (Max)	Transparency	Self-healing property	Conformability (Young's modulus)	Strain sensing	Temperature -sensing	Humidity-sensing	Moist-electric-generating	Ref.
PMAA-co-DMAPS	-	-	-	10000%	＞90%	Yes	Yes	Yes	(10-90℃)	-	-	13
PAA/PDMAEA-Q	Yes	-	-	10000%	＞90%	Yes	Yes	Yes	(5-95℃)	(5-70 RH%)	V_{Max}=70 mV	14
Ag/TA@CNC /borax/ PVA	-	-	-	4000%	-	Yes	465.56 kPa	Yes	-	-	-	15
HLPs/P(AAm-co-LMA)	-	-	-	2058%		-	53 kPa	Yes	-	-	-	16
AMP-regulated/PAAm	-	-	-	2160%	-	-	25 kPa	Yes	-	-	-	17
P(AA-co-DMAPS)/NaCl	-	-	-	10000%	＞90%	Yes	Yes	Yes	(10-90℃)	-	-	18
HP(AAm/AA)-CS-Fe³⁺	-	-	-	1250%	-	-	-	Yes	-	-	-	19
k-carrageenan/PAM DN organohydrogel	Yes	Yes	-	1225%	∼85%	Yes	-	Yes	-	(4-90 RH%)	-	12
Fe₃O₄@PAA/PAA ionogel	Yes	-28℃	-	1400%	-	Yes	35 kPa	Yes	-	-	-	20
PDMAPS/PAA/IL	-	-10℃	-	10000%	＞90%	Yes	Yes	Yes	(-10-100℃)	(5-70 RH%)	V_{Max}=50 mV	21
Graphene–PAA–ACC	-	-	-	500%	-	Yes	Yes	Yes	-	-	-	22
PVA-PAM/KCl	-	-	Yes	500%	∼82%	-	-	Yes	-	-	-	23
PAA/TA@CNC/Fe³⁺	-	-	-	2900%	Yes	Yes	48.5 kPa	Yes	-	-	-	24
PVA-PEDOT: PSS organohydrogel	Yes	-55℃	-	1000%	-	Yes	331 kPa	Yes	-	-	-	7
NaCl/SA/PAM	-	-	-	3120%	99.6%	-	650 kPa	Yes	-	-	-	25
ACC/PAA/alginate mineral	-	-	-	1000%	-	Yes	6.7 kPa	Yes	-	-	-	26
PDMA/NaCl/SDS	-	-	-	-	∼80%	-	-	Yes	(5-50℃)	-	-	27
P(AAm-co-HEMA)/PANI	-	-	-	430%	-	-	200 kPa	Yes	-	-	-	28
PAA–GO–Ca²⁺	-	-	-	2500%	-	Yes	~753.667 kPa	Yes	-	-	-	29
This work	**Yes**	**-63.28℃**	**27.85%**	**450%**	**93.8%**	**Yes**	**Yes (76 kPa)**	**Yes**	**(-30-70℃)**	**(45-85 RH%)**	**V_{Max}=169.1 mV**	

"-": Not available or not mentioned in references.

Note S1.

The table above details the structure and performance of our hydrogel-based biomimetic skin compared to those from recent outstanding publications. Although the as-prepared hydrogel does not exhibit very high stretchability, it can meet the actual requirements, or fit closely to the natural skin. In particular, the Young's modulus of the editable kirigami strain sensor based on the hydrogel is virtually close to the range of human skin modulus (25-220 kPa). Meanwhile, we also introduced the concept of softness for the first time for hydrogels, and conceptually proved that hydrogel is a suitable material for preparing bionic skin compared to other polymer materials. In addition, the high durability (anti-freeze and anti-dryness) is favorable to extend the life of bionic skin. The improvements of hydrogel transparency and haze are also crucial for the realization of visualization and personal medicine. More importantly, we have simultaneously achieved multiple sensing (temperature, humidity, and strain) and the detection of -30℃ by adding glycerol and Ca^{2+} in the hydrogel. Most impressively, the hydrogel-based moist-electric generator produces voltage up to 169.1 mV, which is much higher than that from previous works.

In addition, we try to solve the puzzle of recognizing complex and changing signals at the same time. First, the pressure/strain sensor can be covered with a VHB tape to reduce the effects of moisture signals. It can also be assembled into a capacitive sensor to reduce the effect of temperature signals. The temperature sensor is attached to the flat position of the arm to isolate the strain signal interference. Moreover, a VHB tape is coated on the sensor surface to prevent moisture interference. The humidity sensor is

attached to the flat position of the arm to isolate the strain signal interference. However, the moisture sensor in the work can achieve accurate humidity sensing only under a stable temperature environment. The human skin will also inevitably be affected by temperature when it recognizes moisture, such as high-temperature or low-temperature moisture.

Therefore, we will explore some new signal response mechanisms in the future work, which only respond to a single stimulus.

Table S2. The comparison of voltage from polymer gel-based and cellulose-based moist-electric generation systems.

Materials	Voltage (mV)	Reference
PAA/PDMAEA-Q hydrogel	*70*	*14*
PDMAPS/PAA/IL Hydrogel	*50*	*21*
Cellulose aerogel	*110*	*30*
PVA/cellulose organohydrogel	**169.1**	This work

References:

1. Delley, B., *J. Chem. Phys.* 1990, 92, (1), 508-517.

2. Delley, B., *J. Chem. Phys.* 2000, 113, (18), 7756-7764.

3. Perdew, J. P.; Wang, Y., *Phys. Rev. B* 1992, 45, (23), 13244-13249.

4. Ortmann, F.; Bechstedt, F.; Schmidt, W. G., *Phys. Rev. B* 2006, 73, (20), 205101.

5. Han, L.; Liu, K.; Wang, M.; Wang, K.; Fang, L.; Chen, H.; Zhou, J.; Lu, X., *Adv. Funct. Mater.* 2018, 28, (3), 1704195.

6. Hu, C.; Zhang, Y.; Wang, X.; Xing, L.; Shi, L.; Ran, R., Stable, *ACS Appl. Mater. Interfaces* 2018, 10, (50), 44000-44010.

7. Rong, Q.; Lei, W.; Chen, L.; Yin, Y.; Zhou, J.; Liu, M., *Angew. Chem., Int. Ed.* 2017, 56, (45), 14159-14163.

8. Pan, X.; Wang, Q.; Guo, R.; Ni, Y.; Liu, K.; Ouyang, X.; Chen, L.; Huang, L.; Cao, S.; Xie, M., *J. Mater. Chem. A* 2019, 7, (9), 4525-4535.

9. Yang, Y.; Guan, L.; Li, X.; Gao, Z.; Ren, X.; Gao, G., *ACS Appl. Mater. Interfaces* 2019, 11, (3), 3428-3437.

10. Wang, Q.; Pan, X.; Lin, C.; Lin, D.; Ni, Y.; Chen, L.; Huang, L.; Cao, S.; Ma, X., *Chem. Eng. J.* 2019, 370, 1039-1047.

11. Pan, X.; Wang, Q.; He, P.; Liu, K.; Ni, Y.; Ouyang, X.; Chen, L.; Huang, L.; Wang, H.; Tan, Y., *ACS Sustainable Chem. Eng.* 2019, 7, (8), 7918-7925.

12. Wu, J.; Wu, Z.; Xu, H.; Wu, Q.; Liu, C.; Yang, B.-R.; Gui, X.; Xie, X.; Tao, K.; Shen, Y.; Miao, J.; Norford, L. K., *Mater. Horiz.* 2019, 6, (3), 595-603.

13. Z. Lei, P. Wu, *ACS Nano* 2018, 12, 12860.

14. Z. Lei, P. Wu, *Mater. Horiz* 2019, 6, 538.

15. F. Lin, Z. Wang, Y. Shen, L. Tang, P. Zhang, Y. Wang, Y. Chen, B. Huang, B. Lu, *J. Mater. Chem. A* 2019, 7, 26442.

16. S. Xia, Q. Zhang, S. Song, L. Duan, G. Gao, *Chem. Mater.* 2019, 31, 9522.

17. Q. Zhang, X. Liu, X. Ren, F. Jia, L. Duan, G. Gao, *Chem. Mater.* 2019, 31, 5881.

18. Z. Lei, P. Wu, *Nat. Commun. 2*018, 9, 1134.

19. J. Xu, R. Jin, X. Ren, G. Gao, *J. Mater. Chem. A* 2019, 7, 25441.

20. L. M. Zhang, Y. He, S. Cheng, H. Sheng, K. Dai, W. J. Zheng, M. X. Wang, Z. S. Chen,

Y. M. Chen, Z. Suo, *Small* 2019, 15, 1804651.

21. Z. Lei, P. Wu, *Nat. Commun.* 2019, 10, 3429.

22. S. Lin, X. Zhao, X. Jiang, A. Wu, H. Ding, Y. Zhong, J. Li, J. Pan, B. Liu, H. Zhu, *Small* 2019, 15, 1900848.

23. G. Ge, Y. Zhang, J. Shao, W. Wang, W. Si, W. Huang, X. Dong, *Adv. Funct. Mater.* 2018, 28, 1802576.

24. C. Shao, M. Wang, L. Meng, H. Chang, B. Wang, F. Xu, J. Yang, P. Wan, *Chem. Mater.* 2018, 30, 3110.

25. X. Zhang, N. Sheng, L. Wang, Y. Tan, C. Liu, Y. Xia, Z. Nie, K. Sui, *Mater. Horiz.* 2019, 6, 326.

26. Z. Lei, Q. Wang, S. Sun, W. Zhu, P. Wu, *Adv. Mater.* 2017, 29, 1700321.

27. Z. Lei, Q. Wang, P. Wu, *Mater. Horiz.* 2017, 4, 694.

28. Z. Wang, J. Chen, Y. Cong, H. Zhang, T. Xu, L. Nie, J. Fu, *Chem. Mater.* 2018, 30, 8062.

29. Y. Wang, Q. Chang, R. Zhan, K. Xu, Y. Wang, X. Zhang, B. Li, G. Luo, M. Xing, W. Zhong, *J. Mater. Chem. A* 2019, 7, 24814.

30.   M. Li, L. Zong, W. Yang, X. Li, J. You, X. Wu, Z. Li, C. Li, *Adv. Funct. Mater.* 2019, 29, 1901798;